The first ground-based detection of the 752 GHz water line in local ultraluminous infrared galaxies using APEX-SEPIA

Citation for the original published paper (version of record):
Quinatoa, D., Yang, C., Ibar, E. et al (2024). The first ground-based detection of the 752 GHz water line in local ultraluminous infrared
galaxies using APEX-SEPIA. Monthly Notices of the Royal Astronomical Society, 527(3): 6321-6331. http://dx.doi.org/10.1093/mnras/stad3441

Monthly Notices of the ROYAL ASTRONOMICAL SOCIETY

MNRAS **527,** 6321–6331 (2024) https://doi.org/10.1093/mnras/stad3441
Advance Access publication 2023 December 4

The first ground-based detection of the 752 GHz water line in local ultraluminous infrared galaxies using APEX-SEPIA

Daysi Quinatoa,[1★] Chentao Yang ,[2★] Edo Ibar,[1] Elizabeth Humphreys,[3,4] Susanne Aalto,[2] Loreto Barcos-Muñoz,[5,6] Eduardo González-Alfonso,[7] Violette Impellizzeri,[8] Yara Jaffé ,[1,9] Lijie Liu ,[10,11] Sergio Martín ,[3,4] Axel Weiss[12] and Zhi-Yu Zhang [13,14]

[1]Instituto de Física y Astronomía, Universidad de Valparaíso, Avda. Gran Bretaña 1111, Valparaíso, Chile
[2]Department of Earth and Space Sciences, Chalmers University of Technology, Onsala Observatory, SE-439 94 Onsala, Sweden
[3]Joint ALMA Observatory, Alonso de Córdova 3107 Vitacura, Santiago 763-0355, Chile
[4]European Southern Observatory, Alonso de Córdova, 3107, Vitacura, Santiago 763-0355, Chile
[5]National Radio Astronomy Observatory, 520 Edgemont Road, Charlottesville, VA 22903, USA
[6]Department of Astronomy, University of Virginia, 530 McCormick Road, Charlottesville, VA 22903, USA
[7]Departamento de Física y Matemáticas, Universidad de Alcalá, Campus Universitario, E-28871 Alcalá de Henares, Madrid, Spain
[8]Leiden Observatory, Leiden University, PO Box 9513, NL-2300 RA Leiden, the Netherlands
[9]Departamento de Física, Universidad Técnica Federico Santa María Casilla 110-V, Valparaíso, Chile
[10]Cosmic Dawn Center (DAWN), Denmark
[11]DTU-Space, Elektrovej, Building 328, DK-2800 Kgs. Lyngby, Denmark
[12]Max-Planck-Institut für Radioastronomie, Auf dem Hügel 69, D-53121 Bonn, Germany
[13]School of Astronomy and Space Science, Nanjing University, Nanjing 210023, P. R. China
[14]Key Laboratory of Modern Astronomy and Astrophysics (Nanjing University), Ministry of Education, Nanjing 210023, P. R. China

Accepted 2023 November 3. Received 2023 October 30; in original form 2023 August 23

ABSTRACT

We report the first ground-based detection of the water line p-H_2O (2_{11}–2_{02}) at 752.033 GHz in three z < 0.08 ultraluminous infrared galaxies (ULIRGs): IRAS 06035-7102, IRAS 17207-0014, and IRAS 09022-3615. Using the Atacama Pathfinder EXperiment (APEX), with its Swedish-ESO PI Instrument for APEX (SEPIA) band-9 receiver, we detect this H_2O line with overall signal-to-noise ratios of 8–10 in all three galaxies. Notably, this is the first detection of this line in IRAS 06035-7102. Our new APEX-measured fluxes, between 145 and 705 Jy km s^{-1}, are compared with previous values taken from *Herschel* SPIRE FTS. We highlight the great capabilities of APEX for resolving the H_2O line profiles with high spectral resolutions while also improving by a factor of two the significance of the detection within moderate integration times. While exploring the correlation between the p-H_2O(2_{11}–2_{02}) and the total infrared luminosity, our galaxies are found to follow the trend at the bright end of the local ULIRG's distribution. The p-H_2O(2_{11}–2_{02}) line spectra are compared to the mid-*J* CO and HCN spectra, and dust continuum previously observed with ALMA. In the complex interacting system IRAS 09022-3615, the profile of the water emission line is offset in velocity with respect to the ALMA CO(J = 4–3) emission. For IRAS 17207-0014 and IRAS 06035-7102, the profiles between the water line and the CO lines are spectroscopically aligned. This pilot study demonstrates the feasibility of directly conducting ground-based high-frequency observations of this key water line, opening the possibility of detailed follow-up campaigns to tackle its nature.

Key words: ISM: molecules – galaxies: ISM – infrared: galaxies.

1 INTRODUCTION

Ultra-Luminous InfraRed Galaxies (ULIRGs; with total infrared luminosity $L_{\rm IR}$ between $10^{12}\,L_{\odot}$ and $10^{13}\,L_{\odot}$) are part of the most extreme galaxy populations in the nearby Universe (Sanders et al. 2003). They are characterized to be rich in dust and molecular gas (e.g. Solomon et al. 1997; Genzel et al. 1998; Greve et al. 2005) and to have higher gas fractions compared to normal star-forming galaxies (Gao & Solomon 2004). ULIRGs are mostly late-stage mergers (e.g. Sanders & Mirabel 1996) understood as a transitional phase in the evolution of galaxies, passing through a brief starburst phase triggered by a major interaction that cause the in-falling of the interstellar medium (ISM) to the innermost regions, likely triggering nuclear starburst and active galactic nuclei (AGNs) but with complex evolution links between the two (e.g. Farrah et al. 2001; Lonsdale, Farrah & Smith 2006). After the molecular gas is consumed, they

★ E-mail: daysi.quinatoa@postgrado.uv.cl (DQ); chentao.yang@chalmers.se (CY)

will probably end up as passive galaxies hosting supermassive black holes in their centres. Therefore, ULIRGs offer unique insights into our understanding of galaxy evolution. To describe their nature, it is imperative to understand why they have such intense, compact star formation, and what powers the nuclear star formation activity. The majority of the radiation produced in their nuclei, whether by an AGN or by star formation, is absorbed by dust and re-emitted in the far-infrared (far-IR). Because of the intense obscuration, identifying the predominant power source of local ULIRGs is challenging. Using emission lines from molecules such as OH and H_2O, whose excitation depend on the far-IR continuum photons, could be a potential diagnostic to distinguish AGN from starburst activity (González-Alfonso et al. 2010; van der Werf et al. 2011; Pensabene et al. 2022; Decarli et al. 2023).

H_2O is the third most abundant molecule in the ISM, either in the gas phase in warm regions or in the solid phase on dust mantles (e.g. van Dishoeck, Herbst & Neufeld 2013), and serves as one of the most important coolants of the cold molecular gas (Neufeld, Lepp & Melnick 1995). In particular, the thermal para-$H_2O(2_{11}–2_{02})$ line is emitted at 752.033 GHz rest-frame and has an upper energy level of $E_{up}/k_B = 136.9$ K. In Galactic star forming regions, this line is predominantly originated by shocks that trace high density and temperature gas (e.g. Mottram et al. 2014; van Dishoeck et al. 2021). On the other hand, surveys of submillimetre (submm) H_2O lines with *Herschel* in local galaxies revealed that this water line is one of the brightest submm H_2O lines (Yang et al. 2013; Lu et al. 2017). The modelling of water in galaxies, assuming different phases of the ISM, with different dust temperatures, shows that this line comes predominantly from the warm phase with $T_{dust} \sim 45$–75 K (González-Alfonso et al. 2014). The p-$H_2O\,(2_{11}–2_{02})$ line can be excited via collision in warm dense conditions with a column density of $N_{H_2O} \sim (0.5 - 2) \times 10^{17}$ cm^{-2}, sharing a common spatial distribution with those regions traced by mid-*J* CO lines in star-forming galaxies (González-Alfonso et al. 2014; Liu et al. 2017). Additionally, H_2O lines can be excited radiatively by far-IR photons. This so-called pumping mechanism of p-$H_2O\,(2_{11}–2_{02})$ is induced by the 101 μm continuum, which excites the H_2O molecules from the base energy level 1_{11} to 2_{20}. This level 2_{20} then cascades down to 2_{11} and later to 2_{02} producing line emission at 1229, 752, and 988 GHz, respectively. Furthermore, the combination of far-IR 75 μm absorption ortho-$H_2O\,(3_{21}–2_{12})$ and the $3_{21}–3_{12}$ 1163 GHz emission enhance the radiative excitation for the submm lines with $E_{up}/k_B < 300$ K, including the 752 GHz one (González-Alfonso et al. 2022). The p-$H_2O\,(2_{11}–2_{02})$ far-IR pumping makes H_2O lines a prominent tracer of the conditions of the far-IR field, especially in highly obscured regions of galaxies (e.g. González-Alfonso et al. 2014). Previous studies have shown that the p-$H_2O\,(2_{11}–2_{02})$ is well correlated with the total infrared luminosity in both local and high-redshift galaxies (Omont et al. 2013; Yang et al. 2013, 2016; Jarugula et al. 2019; Berta et al. 2023). The nearly linear correlation between L_{H_2O} and L_{IR} lines suggest that water can be excited to high energy levels by far infrared pumping and provides another approach for tracing the far infrared field in star-forming galaxies. The correlation can be a natural consequence of far-IR pumping H_2O excitation (González-Alfonso et al. 2014).

In dusty star-forming galaxies, H_2O lines trace both, the properties of the molecular gas and the dust content, offering a powerful tool to study their physical nature. This becomes especially important in ULIRGs as they present ideal conditions for water emission, intense far-IR radiation fields, and warm dense gas content. In fact, the H_2O lines can offer unique insights into the innermost dust-obscured regions with very high opacity, providing essential information on the ISM physical conditions of the most extreme ULIRGs (e.g. Falstad et al. 2017; Liu et al. 2017; Yang et al. 2020; González-Alfonso et al. 2021), where often the p-$H_2O\,(2_{11}–2_{02})$ line becomes optically thick (e.g. González-Alfonso et al. 2014).

Although thermal H_2O lines provide powerful line diagnostics, their detection from ground-based observatories is impeded by the presence of water vapour in the Earth's atmosphere, which significantly reduces atmospheric transmission. From space, the H_2O lines have been studied in large samples of far-IR bright galaxies with limited spectral resolutions with *Herschel Space Observatory* SPIRE-FTS (e.g. Yang et al. 2013; Pearson et al. 2016), despite a handful of sources studied with high-spectral resolution with *Herschel* HIFI (Liu et al. 2017). It is known that the p-$H_2O\,(2_{11}–2_{02})$ line is ubiquitous in the spectra of molecular clouds in the Milky Way and local galaxies, but it has also been found to be a prominent emission line amongst the water lines detected in high-redshift infrared bright galaxies, both unlensed (e.g. Gullberg et al. 2016; Riechers et al. 2017; Casey et al. 2019; Lehnert et al. 2020; Li et al. 2020; Pensabene et al. 2021; Stanley et al. 2021) and gravitationally amplified (e.g. Bradford et al. 2011; Lis et al. 2011; Omont et al. 2011; Combes et al. 2012; Bothwell et al. 2013; Omont et al. 2013; Riechers et al. 2013; Yang et al. 2016; Apostolovski et al. 2019; Jarugula et al. 2019; Yang et al. 2019a, b, 2020; Berta et al. 2021; Jarugula et al. 2021). The similarity found in profiles between water and mid-*J* to high-*J* level CO transitions strongly suggests that water emission originates from regions of active star formation (e.g. see fig. 13 from Yang et al. 2017). Exploring the properties of water lines then becomes a key aspect for characterizing the cosmic star formation history of the Universe.

It is important to highlight that most of the detected submm water lines from local galaxies have been made by *Herschel* (see Weiß et al. 2010; Yang et al. 2013; Liu et al. 2017), nevertheless as this is no longer available, and until the next generation of far-infrared space telescopes, exploiting ground-based submm facilities are the only possibility to explore high-frequencies to measure water lines with high spectral resolution and, in the case of ALMA, unprecedented angular resolution.

In this work, we present high-spectral resolution observations of the p-$H_2O\,(2_{11}–2_{02})$ in three low-redshift ULIRGs (IRAS 06035-7102, IRAS 17208-0014, and IRAS 09022-3615) using the single-dish APEX telescope with the SEPIA receiver in Band-9 (Baryshev et al. 2015; Belitsky et al. 2018). Throughout this work, we assumed a ΛCDM cosmology with $\Omega_M = 0.3$, $\Omega_\Lambda = 0.7$, and $H_0 = 75$ km s^{-1} Mpc^{-1}.

2 DATA

2.1 Source selection

The three sources were selected from a sample of ULIRGs observed in water lines with *Herschel* and presented in Yang et al. (2013). From this sample, we selected the sources below declination +25° and, in order to ensure a good atmospheric transmission, we excluded sources whose observed water line p-$H_2O\,(2_{11}–2_{02})$ (752.033 GHz rest-frame) frequencies are higher than 722 GHz. Eight ULIRGs fulfil the selection criteria. Based on integration time estimates, considering expected line fluxes and atmospheric transmission, as a pilot project, we chose to target three sources, IRAS 17207-0014, IRAS 06035-7102, and IRAS 09022-361. These three sources maximized the detection of the water line within a short integration time.

Table 1. Observed H_2O (2_{11}–2_{02}) line parameters.

N	Source	RA (J2000)	Dec (J2000)	z	ν_{obs} (GHz)	D_L (Mpc)	$FWHM_{H_2O}$ (km s^{-1})	$S_{H_2O}\,\Delta v$ (Jy km s^{-1})	L_{H_2O} ($L_\odot/10^6$)	t_{int} (h)
	(1)	(2)	(3)	(4)	(5)	(6)	(7)	(8)	(9)	(10)
1	IRAS 06035-7102	06:02:54.01	−71:03:10.2	0.07946	696.7	325.0	414.88 ± 54.01	145.73 ± 16.32	10.33 ± 1.16	12.3
2	IRAS 17208-0014	17:23:21.96	−00:17:00.9	0.04281	721.2	175.68	515.90 ± 68.61	704.77 ± 83.72	15.64 ± 1.86	4.2
3	IRAS 09022-3615	09:04:12.71	−36:27:01.0	0.05964	709.7	238.84	414.81 ± 49.89	199.08 ± 20.84	7.90 ± 0.83	14.3

Note. (1) Source name. (2) Right ascension. (3) Declination. (4) redshift from the NASA/IPAC Extragalactic Database (NED). (5) Central observed frequency. (6) Luminosity distance in Mpc from Yang et al. (2013). (7) The H_2O (2_{11}–2_{02}) FWHM. (8) The velocity-integrated flux density. (9) Line luminosity. (10) Total APEX integration time (including overheads).

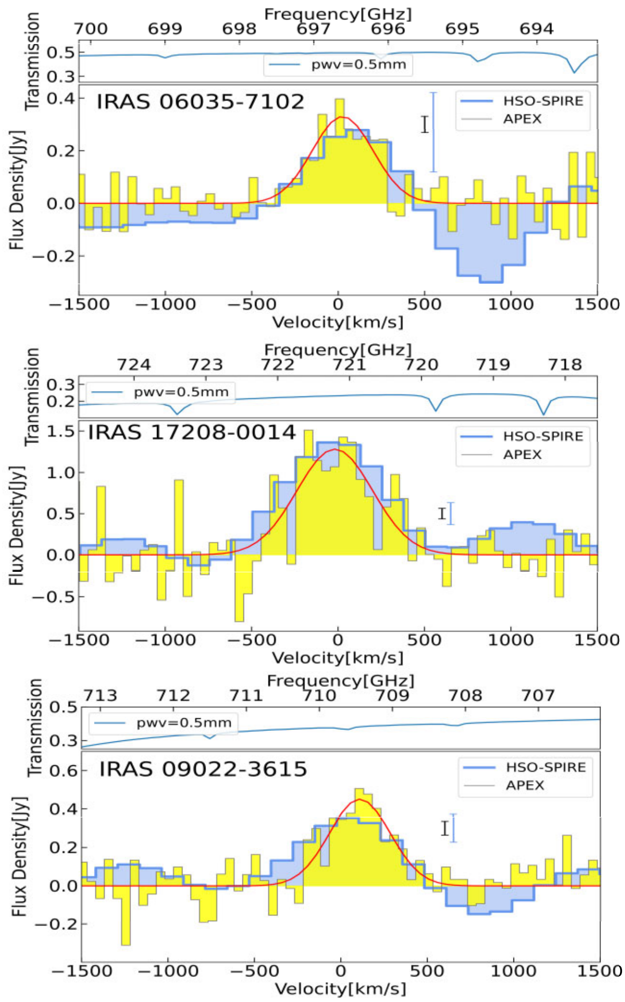

Figure 1. Redshifted para-H_2O(2_{11}–2_{02}) at 752.033 GHz emission line for the three ULIRGs presented in this work. The spectra have been centred according to the redshift in Table 1. The histograms show the binned APEX spectra, while the solid line correspond to Gaussian fits. Overplotted are the unapodized *Herschel* SPIRE-FTS spectra. Error bars show a comparison between uncertainties within a bandwidth of 40 GHz, in both spectra after considering a convolution of the APEX spectra with the SPIRE-FTS instrumental line spread function. The upper panel shows the atmospheric transmission for SEPIA 660 at PWV of 0.5 mm at an elevation of 55°.

2.2 Observations

We observed IRAS 06035-7102 ($z = 0.07946$), IRAS 17208-0014 ($z = 0.04281$), and IRAS 09022-3615 ($z = 0.05964$) with APEX SEPIA-660 Band 9 receiver (Project: E-0103.B-0471A-2018, PI: C. Yang) operating at the observing frequency range of ∼ 690–725 GHz. The APEX beam size at this frequency is 9.″5. Observations were carried out between 2019 May 11–12, June 03, 22–24, and August 21–22, 27–29. The ON-OFF observations were performed in the wobbler-switching symmetric mode with an amplitude of 40 arcsec and a wobbling rate of 1.5 Hz. The Doppler correction to account for the motion of the Earth was applied during the observations. R-Dor and L2-Pup were used for pointing and focus calibration. The focus was checked at the beginning of each observing session, and pointing was checked every approximately 1.5 h. Spectral setup covers 8 GHz per sideband and a separation of 8 GHz between the upper- and lower-side bands. The observation was centred on the redshifted line frequency of interest, and we requested a line peak-to-rms ratio of S/N>5 in velocity channels of ∼50 km s^{-1}. The precipitable water vapour (PWV) during the observations varied between 0.4 and 0.9 mm, corresponding to typical atmospheric transmission of 60 per cent and 20 per cent, respectively. The total integration times ranged between 4 and 15 h per target (Table 1).

2.3 Data reduction

The data were reduced using the GRENOBLE IMAGE AND LINE DATA ANALYSIS SOFTWARE (GILDAS)[1] – CONTINUUM AND LINE ANALYSIS SINGLE-DISH SOFTWARE (CLASS) package. For each target, we collected all the scans for different observing dates. For each observing date, we checked all the individual scans and discarded those affected by anomalous noise levels or weather conditions as noted by the log-file of the observations. For each scan, we masked a velocity window from −500 to +500 km s^{-1} centred at the expected line observing frequency to fit a second-order polynomial subtraction, which accounts better for the baseline shapes, to remove the baseline out of the spectra. Then we combined all of the individual spectra, using noise-based weighing and aligning them at the frequency of interest. We have also explored the baseline subtraction using first-order polynomials and did not find any major differences compared with the second-order polynomial fits.

To display the spectra, we use a spectral resolution of 50 km s^{-1}channel width (see Fig. 1). Considering the antenna temperature T_A^* corrected for the atmospheric attenuation, the forward efficiency and signal band gain, we derive flux densities using a conversion factor of 75 ± 6 Jy K^{-1} measured during the observations period with SEPIA-660.[2] The measured noise root mean squared (RMS), for all three sources, ranges between 77 and 340 mJy beam^{-1}. The final spectra were exported to Python for the remaining analysis. IRAS 17208-0014 became the brightest source, so less integration

[1] https://www.iram.fr/IRAMFR/GILDAS/
[2] https://www.apex-telescope.org/telescope/efficiency/

time was needed to reach the requested signal-to-noise ratios (see Table 1).

2.4 SED photometry

Previous analyses indicate that the p-H_2O (2_{11}–2_{02}) is likely to be dominated by far-IR pumping excitation by the photons at 101 µm (e.g. González-Alfonso et al. 2022). If this is the case for our sources, we would expect a tight correlation between H_2O emission and far-IR dust continuum. In order to further explore this, we re-analysed the *Herschel* Photodetector Array Camera and Spectrometer (PACS) 100 µm emission of IRAS 17208-0014 (Obslist:1342241375, 1342241376) and IRAS 09022-3615 (Obslist:1342233593, 1342233594). These were retrieved from the *Herschel* Public Archive (programme OT1, PI: D. Sanders). Each galaxy was observed in cross-scanning mode at 20 arcsec s^{-1} and UNIMAP projected maps were considered. Since PACS simultaneously observes at 100 and at 160 µm, we performed aperture photometry at both wavelengths following the pointSourceAperturePhotometry script using the *Herschel* Interactive Processing Environment (HIPE) version 15.0.1 software (Ott 2010). We measured the flux at different aperture radii (up to ∼ 4 × full-width at half-maximum, FWHM) and checked the aperture at which the encircled energy fraction stabilizes. This profile is compared to the point spread function profile finding that both behave similarly, concluding that the two far-IR sources are point-like at the *Herschel* PACS beam (FWHM ∼ 6.″7 × 6.″9 for 100 µm and ∼ 10.″6 × 12.″1 for 160 µm). The photometric error is estimated using six equal apertures placed in the background around the source. The results for this aperture photometry are in agreement with those presented by Chu et al. (2017).

Using photometric points from the *Wide-field Infrared Survey Explorer* (*WISE*) 22 µm, the Infrared Astronomical Satellite (IRAS) 60 µm, PACS 70 µm, and *Herschel* SPIRE 250, 350, and 500 µm, for all three sources we construct the spectral energy distribution (SED) to estimate their total infrared luminosities $L_{\rm IR}$ (see Table A1 for the details).

2.5 Ancillary submm data

Public ALMA observations of CO(J = 4–3) and 630 µm dust continuum were retrieved for IRAS 09022-3615 and IRAS 17208-0014 (project ID: 2018.1.00994.S, PI: T. Michiyama). For IRAS 06035–7102, we retrieved data from HCN(J = 2–1) (project ID:2017.1.00022.S, PI: M. Imanishi) and from CO(J = 3–2) and 850 µm dust continuum (project ID:2018.1.00503.S, PI: A. Gowardhan). All observations were reduced using the standard pipeline calibration scripts provided by ALMA with the Common Astronomy Software Applications (CASA; CASA Team 2022) for the respective cycles. After obtaining the calibrated measurement sets, the imaging process was done with the task TCLEAN. We created an initial datacube where we identified the line-free channels. For the continuum subtraction, we used the task UVCONTSUB. We ran the cleaning process down to 1 σ using interactive masks located at the source positions. The spectral resolution of the cubes is set to 50 km s^{-1}, using a natural weighting and a primary-beam corrected map. To better compare the p-H_2O (2_{11}–2_{02}) line to the ALMA CO(J = 4–3), CO(J = 3–2), and HCN(J = 2–1) observations, the ALMA data cubes were degraded in spatial resolution down to the same APEX beam using the task IMSMOOTH. The final ALMA spectra used for comparison are extracted at the convolved central brightest pixel in Jy beam^{-1} units (Fig. 1).

Table 2. A comparison of the velocity integrated p-H_2O (2_{11}–2_{02}) flux densities $S_{H_2O}\Delta v$ between our results and previous ones with *Herschel* SPIRE-FTS taken from the literature.

Source	APEX (Jy km s^{-1})	HSO-SPIRE (Jy km s^{-1}) Yang et al. (2013)	HSO-SPIRE (Jy km s^{-1}) Pearson et al. (2016)
1	145.73 ± 16.32	<411*	
2	704.77 ± 83.72	697.98 ± 88.70	654.23 ± 57.40**
3	199.08 ± 20.84	184.65 ± 52.32	165.95 ± 40.68**

Note. *The value is a 3-σ upper limit, although the original work reports a < 3 σ tentative detection of 408.63 ± 136.98 Jy km s^{-1} with low significance. ** The conversion factor from W m^{-2} to Jy km s^{-1} is assumed Q = 3 × $10^{22}/\nu_{\rm rest}$(GHz).

3 RESULTS AND DISCUSSION

3.1 Water line measurements

Using APEX SEPIA Band-9 we detected the thermal transition of the water molecule p-H_2O (2_{11}–2_{02}) in all three ULIRGs at >8σ significance levels. For IRAS 06035-7102, this is the first clear detection of p-H_2O (2_{11}–2_{02}), superseding the tentative ∼3σ detection reported by Yang et al. (2013). The spectra of p-H_2O (2_{11}–2_{02}) observed with APEX toward IRAS 06035-7102, IRAS 17208-0014, and IRAS 09022-3615 are shown in Fig. 1, in comparison with the low resolution *Herschel* SPIRE-FTS spectra (the full spectra can be seen in Fig. B1). We note that the zero velocity is defined by the redshift of the source, as indicated in Table 1. We have identified a velocity shift of 100 km s^{-1} in the case of IRAS 09022-3615, which will be discussed in detail in Section 3.4. We confirm the line detection at a higher significance (at least a factor of two) and higher spectral resolution. The spectra show that p-H_2O (2_{11}–2_{02}) is detected with a peak flux density of 0.45 ± 0.09 Jy beam^{-1} in IRAS 09022-3615, 1.28 ± 0.34 Jy beam^{-1} in IRAS 17208-0014 and 0.33 ± 0.08 Jy beam^{-1} in IRAS 06035-7102. The velocity-integrated flux densities and a comparison with previous values taken from the literature are presented in Table 2. The values agree within the uncertainties, with the line fluxes and tentative limits measured with the *Herschel* SPIRE-FTS by Yang et al. (2013) and Pearson et al. (2016).

The instrumental line spread function of SPIRE-FTS is a function that redistributes the line flux along the frequency axis (Hopwood et al. 2015), which correlates the channels across the line profiles. On the other hand, as SEPIA is a heterodyne instrument, it does not have this line spread function effect, offering independent channels and demonstrating its power for resolving the line profiles. Thus APEX not only provides an accurate measurement of the line flux but also provides a direct way to recover the true line profiles, revealing further information about the kinematics of the gas.

The high spectral resolution of APEX allows us to resolve the p-H_2O (2_{11}–2_{02}) lines and determine the FWHM in all three galaxies, which are 415, 516, and 415 km s^{-1} for IRAS 06035-7102, IRAS 17208-0014, and IRAS 09022-3615, respectively (Table 1). Within the 9.″5 APEX beam and a spectral resolution of 50 km s^{-1}, the line profiles are consistent with a single Gaussian, facilitating clean measurements of their velocity-integrated flux densities.

To compare the spectral noise between the APEX and the previous *Herschel* SPIRE-FTS measurements, we convolved the APEX spectra with the line spread function profile of SPIRE-FTS and then binned these spectra to match the spectral SPIRE-FTS resolution. The error bars (measured within a 40 GHz bandwidth for both) obtained for the convolved/binned APEX and SPIRE-FTS are shown

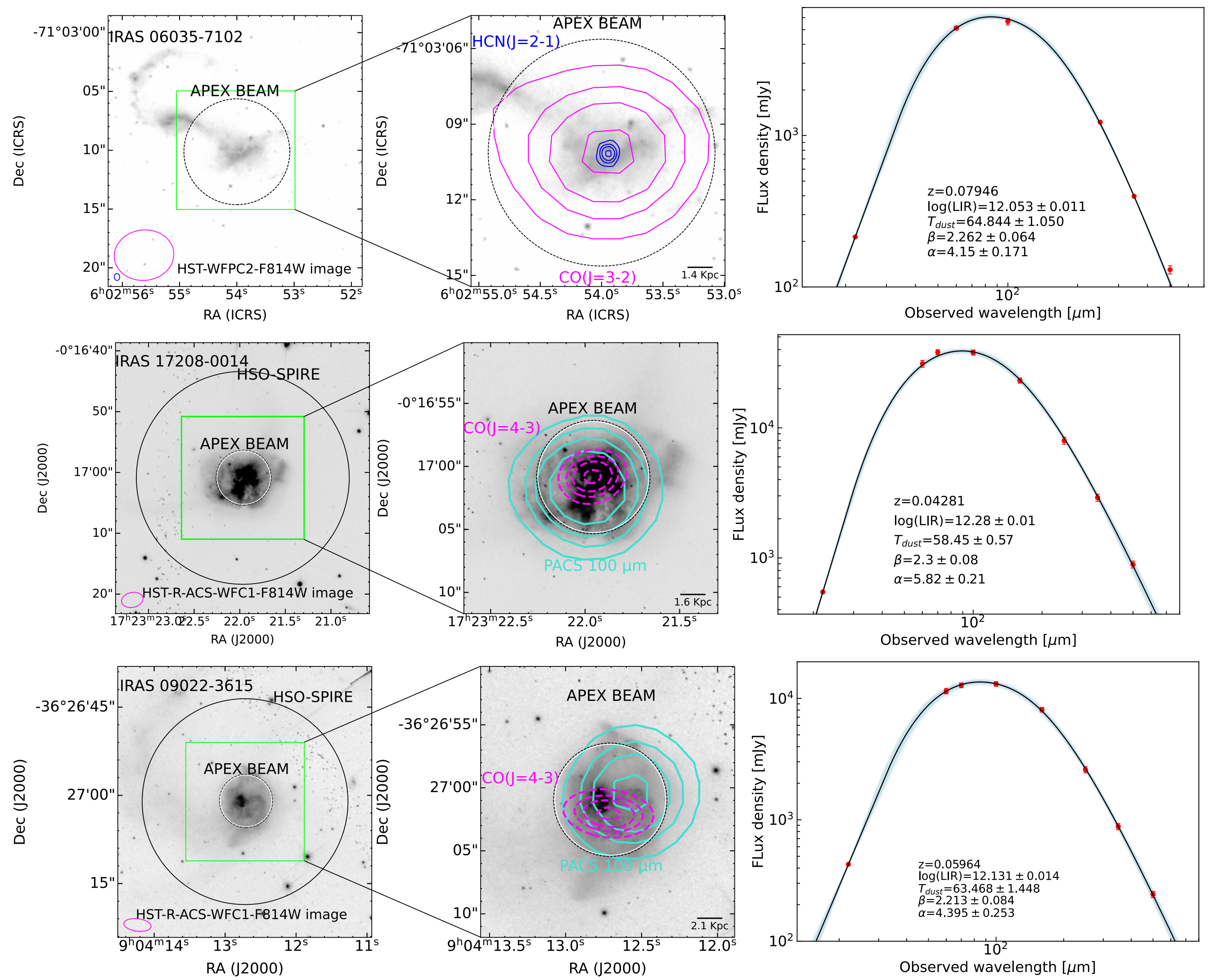

Figure 2. Left: *Hubble Space Telescope R*-band images of the three ULIRGs presented in this work. We use a logarithmic stretch function to enhance the faint emission. The beams of *Herschel* SPIRE (solid circle) and APEX (dashed line) are overlaid. Centre: The contours represent the 20 per cent, 40 per cent, 60 per cent, 90 per cent of the maximum peak intensity at 100 μm from *Herschel* PACS (solid thick line) and CO(J = 3-2) (dashed line), CO(J = 4-3) (dashed line), or HCN(J = 2-1) (solid line) from ALMA. These maps are at their native resolution and their beams are on the lower side of the left hand side figure. Right: The observed far-IR SED for each galaxy, including photometry from *WISE*, IRAS, and *Herschel*. The fitted SED is shown as a solid line, while the shadow shows 1σ uncertainties.

in Fig. 1, demonstrating the higher significance reached by APEX to characterize the p-H_2O (2_{11}–2_{02}) line emission.

To compute the H_2O luminosities, we follow the equation in Solomon & Vanden Bout (2005):

$$L_{H_2O} = 1.04 \times 10^{-3} S_{H_2O} \Delta v \nu_{rest} (1+z)^{-1} D_L^2 [L_\odot], \quad (1)$$

where $S_{H_2O}\Delta v$ is the velocity integrated flux density in units of Jy km s^{-1}, the rest-frame frequency of the line ν_{rest} is related to the observed frequency ν_{obs} as $\nu_{rest} = \nu_{obs}(1+z)$ is in GHz, D_L is the luminosity distance in Mpc, and z is the redshift. Derived luminosities are presented in Table 1.

In Fig. 2, we present a comparison between the APEX (9.″5) and *Herschel* SPIRE-FTS (35 arcsec) beam sizes. As both spectra show similar intensities, we suggest that most of the water emission comes from a compact region smaller than the APEX beam. To look at the optical nature of the sources, we present images from the *Hubble Space Telescope* (HST) with the Advanced Camera for Surveys (ACS), the Wield Field Camera (WFC), and the Wide Field Planetary Camera (WFPC2) from programmes 6346 (WFPC2, PI: K. Borne) and 10 592 (ACS, PI: A. Evans, see Kim et al. 2013) in the *I* filter (F814W, λ = 8333 Å). The *I*-band images of our galaxies have a large field of view (202 arcsec × 202 arcsec) and capture the detailed structure of the galaxies and the full extent of each ULIRG interaction. We can see that IRAS 06035-7102 is an extended interacting double system, separated by a distance of ∼ 10 arcsec (in WFC2 image; Arribas et al. 2008). IRAS 17208-0014 is an advanced merger with two tidal tails towards the south-east and north-west. IRAS 09022-3615 is a late-type merger presenting a tidal tail. While in IRAS 06035-7102 and IRAS 17208-0014, the ALMA mid-*J* CO and HCN(2–1) maps show that the molecular gas is concentrated towards the nuclear region where the far-IR emission peaks, the CO(3–2) emission in IRAS 09022-3615 locates offset from the peak of the *HST* image and the far-IR dust emission, indicating complex ISM structure and kinematics. Our APEX beams are well aligned with the bulk of the compact molecular gas and dust emissions, which should trace the total H_2O emission from our targets.

3.2 The IR luminosities

To estimate the total infrared luminosity ($L_{\rm IR}$), we model the SED of galaxies between 8 and 1000 µm. We use the Monte Carlo InfraRed SED (MCIRSED; Drew & Casey 2022), which fits the data with a function consisting of a mid-infrared (mid-IR) power law and a far-IR modified blackbody. The model has the form

$$S(\lambda) = \begin{cases} N_{\rm pl}\lambda^{\alpha} & : \frac{\partial \log S}{\partial \log \lambda} > \alpha \\ \frac{N_{\rm bb}\left(1-e^{-(\lambda_0/\lambda)^{\beta}}\right)\lambda^{-3}}{e^{hc/\lambda kT}-1} & : \frac{\partial \log S}{\partial \log \lambda} \leq \alpha, \end{cases} \quad (2)$$

where λ is the rest-frame wavelength, α is the mid-IR power-law slope, $N_{\rm pl}$ and $N_{\rm bb}$ are normalization constants, λ_0 is the wavelength where the dust opacity equals unity, β is the dust emissivity index, T is the luminosity-weighted characteristic dust temperature, h, k, and c are Planck, Boltzmann, and the speed of light constants. The two functions connect at the wavelength where the slope of the modified blackbody is equal to the slope of the power-law function. In our model, α characterizes the hot dust emission and is constrained to be between $0 < \alpha < 6$, while on the other hand, β controls the slope in the Rayleigh–Jeans regime and it is constrained to be between 0.5 and 5.0. In Fig. 2, we show the SED fitting and the estimated fitted values. The value of α for the three galaxies is steep (>4.0), consistent with a lack of significant hot dust emission coming from a buried powerful AGN. The value of the emissivity index, less than 2.5, is in agreement with most values in local star-forming galaxies. As expected, the infrared luminosities are higher than $10^{12}\,L_{\odot}$, consistent with being ULIRGs.

3.3 The $L_{\rm IR} - L_{\rm H_2O}$ correlation

In Fig. 3, we present the correlation between $L_{\rm H_2O}$ and $L_{\rm IR}$ as found in local and high redshift galaxies. Our sample is highlighted in red and is part of the brightest low redshift ULIRGs. Previous studies have shown that the $L_{\rm IR}$-$L_{\rm H_2O}$ correlation is slightly superlinear (e.g. Omont et al. 2013; Yang et al. 2013; Jarugula et al. 2019) compared to other water lines with the exception of $H_2O(2_{11}$–$2_{02})$, which is also excited by 101 µm photons. This correlation opens the possibility of using water as a tracer of the far-IR emission and suggests that the IR pumping mechanism is the main responsible for the excitation of water molecules producing the p-H_2O (2_{11}–2_{02}) line at 752 GHz. Nevertheless, studies of local galaxies show that the low-J ($J < 3$) H_2O lines can also be both collisionally and far-IR excited (Liu et al. 2017). One simple approach to hint light on the nature of the exciting mechanism of the p-H_2O (2_{11}–2_{02}) is to compare the spatial distribution of the water emission to that of the dust continuum near 101 µm, compared to other molecular gas tracers, which are well known to be collisionally excited, such as CO(J = 3–2), CO(J = 4–3), or HCN(J = 2–1). However, given that our APEX observations are only consistent with single pointings, we here compare the line profiles as an indication of a common nature, assuming that kinematic structures are associated with similar spatial distributions.

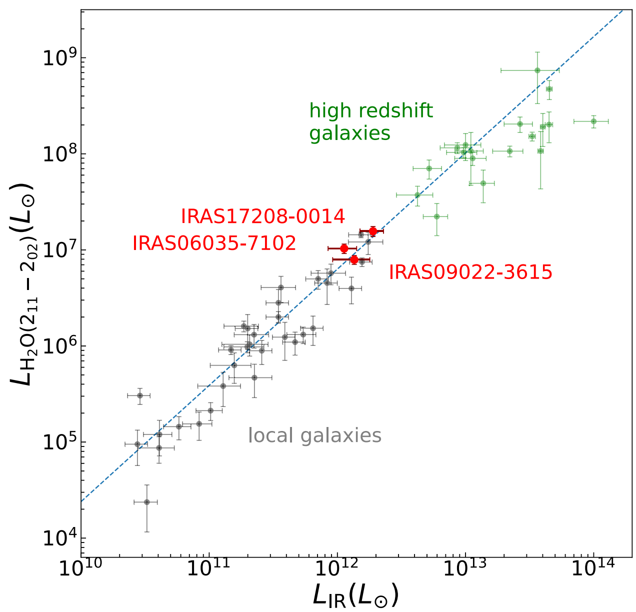

Figure 3. Correlation between $L_{\rm H_2O}$ and $L_{\rm IR}$ in local and high redshift galaxies. The linear correlation by Yang et al. (2013) is shown as a dashed line at $L_{\rm H_2O}/L_{\rm IR} = 5.53 \times 10^{-6}$. The derived values for the three galaxies studied in this paper are depicted as a solid circles. The local galaxy sample and the high-z ULIRGs are taken from Yang et al. (2013, 2016) and Berta et al. (2023).

3.4 Spatial and spectral comparison between H_2O, CO, HCN, and dust

In order to get insights on the origin of the excitation mechanisms of the p-H_2O (2_{11}–2_{02}) emission, in Fig. 2, we present the APEX pointing overplotted on the ALMA CO(J = 3–2), CO(J = 4–3), and HCN(J = 2–1) integrated line contours. Because 101 µm photons are predominantly exciting the H_2O 2_{20} level that relates to the p-H_2O (2_{11}–2_{02}) line (e.g. González-Alfonso et al. 2014; Liu et al. 2017), we explore the spatial distribution of the 100 µm dust continuum using the PACS-100 µm images in relation to that of the H_2O line. We note that the PACS 100 µm emission in IRAS 17208-0014 and IRAS 09022-3615 is point-like (at 9.″5 FWHM ∼ 14 kpc); hence most of the far-IR photons come from the innermost central regions of these ULIRGs. The interferometric ALMA observations towards IRAS 06035-7102 show the HCN(J = 2–1) emission has a deconvolved major axis FWHM of 0.71 ± 0.13 kpc associated with a central region, while the CO(J = 3–2) is spatially aligned with HCN(J = 2–1) presenting a deconvolved major axis FWHM size of 3.1 ± 1.0 kpc. In IRAS 17208-0014, the APEX pointing is centred on the CO(J = 4–3) emission, and the PACS-100 µm emission is centred on the same region. However, in IRAS 09022-3615, we see a significant offset between the peak position of the PACS-100 µm photometry and the CO(J = 4–3) emission (Figs 2, 4, and C1), while at the same time, the APEX pointing is slightly offset with respect to their peaks, located in the redshifted part of the CO emission.

The left panel of Fig. 4 shows a normalized spectroscopic comparison between the p-H_2O (2_{11}–2_{02}), CO(J = 3–2), and CO(J = 4–3) at 50 km s^{-1} channel width. The velocities from ALMA and APEX spectra are under the same frame LSRK (Doppler correction was already applied during the observations). In IRAS 06035-7102, both CO(J = 3–2) and the p-H_2O (2_{11}–2_{02}) emission are spectroscopically aligned. The same is seen for IRAS 17208-0014

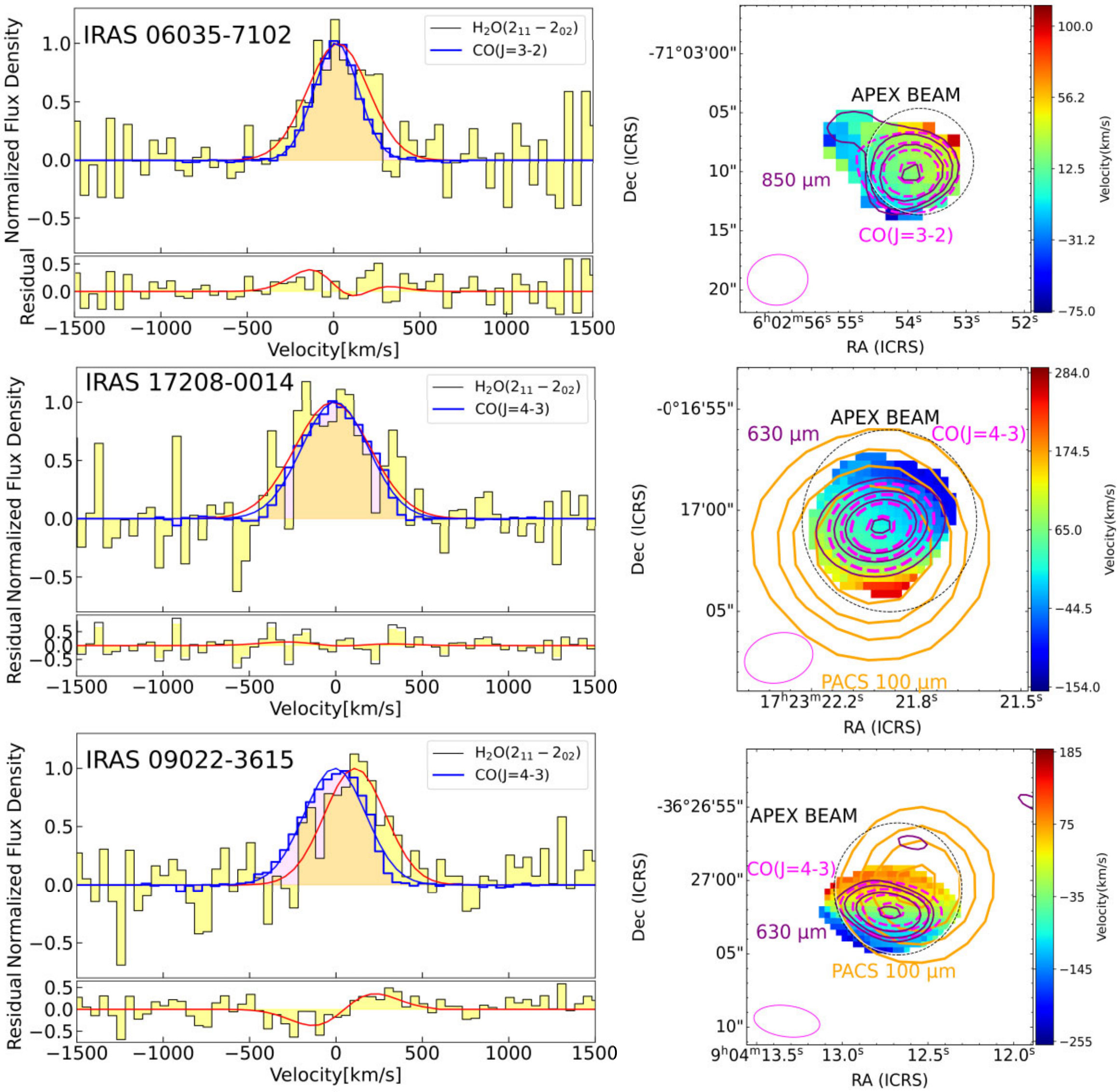

Figure 4. Comparison between the CO(3–2), CO(4–3) line, and the p-H_2O (2_{11}–2_{02}) for the ULIRGs in our sample. Left: Overplotted APEX p-H_2O (2_{11}–2_{02}) and ALMA CO(3–2), CO(4–3) spectra (smoothed to the resolution of the APEX beam before extraction). Both spectra are arbitrarily normalized to the peak of a simple Gaussian fit in order to compare the profiles. In the lower panel, we show the residuals between the profiles and the Gaussian fits. Right: Velocity field (moment 1) of CO(J = 3–2), CO(J = 4–3) (colour bar) compared to the PACS 100 μm dust emission (solid contours) and ALMA intensity CO(J = 4–3) (dashed line) contours, 630 μm (solid contours) and 850 μm (solid contours). The synthesized beams of ALMA CO emission are shown at the bottom left of the right hand side column.

when comparing CO(J = 4–3) and p-H_2O (2_{11}–2_{02}). Nevertheless, in IRAS 09022-3615, we find that the water emission is redshifted compared to the gas traced by CO(J = 4–3). This is best illustrated by the Gaussian fits of the p-H_2O (2_{11}–2_{02}) (red) and CO(J = 4–3) (blue), where we find that H_2O has a peak emission at about +100 km s^{-1} with respect to the systemic velocity defined by the redshift of the sources (see Table 2). This is evident from the residual spectrum, where we can see that there is an excess of water emission in the red part of the spectra at a similar velocity while having a negative peak at the blue part.

The right panel of Fig. 4 shows for IRAS 06035-7102 the intensity and moment 1 map of the CO(J = 3–2) together with the contours of the intensity of dust emission at 850 μm. We show that the APEX pointing is aligned with the 850 μm ALMA dust continuum and with the CO(J = 3–2), suggesting that all the different signals come from the same compact region. For IRAS 17208-0014 and IRAS 09022-3615, we present the intensity and moment 1 map of the CO(J = 4–3) with respect to the contours of the intensity of dust emission of PACS 100 μm and ALMA 630 μm. In IRAS 17208-0014, the CO(J = 4–3), the 100 μm and 630 μm dust continuum are well aligned each other. This suggests that the different tracers are revealing the same dense gas from the very central part of the galaxy. In IRAS 09022-3615, both CO(J = 4–3) and the 630 μm dust continuum are spatially aligned, nevertheless the PACS-100 μm emission is spatially offset by ∼2.″7 (2.9 kpc). If such a spatial offset is real, we might be finding an explanation for the +100 km s^{-1} offset between the p-H_2O (2_{11}–2_{02}) and CO(4–3) lines, where possibly the water line is excited by infrared pumping, via the 101 μm pumping path, at a region different than where the CO line is produced, as the PACS-100 μm emission is peaking at the redshifted part of the CO emission. In this case, the offset between 100 μm (PACS) and 630 μm (ALMA) might be due to temperature/optical-depth variation across the galaxy. After exploring photometric data taken with the *Spitzer Space Observatory* at 8 and 24 μm, we confirm a good alignment between ALMA 630 μm and *Spitzer* data. Considering that PACS photometry lies between these two wavelengths, this suggests instead that the observed offset might be attributed to issues with the astrometric calibration of the *Herschel*-PACS observation. The absolute pointing *Herschel* error in scan maps can range from 0.″9 to 2.″36 (see table 5 of Sánchez-Portal et al. 2014), an uncertainty which is not consistent but varies at each specific observing epoch subject to unique conditions. Our observed spatial offset is approximately the upper limit of the astrometric error. If the offset is indeed caused by the astrometric error, nevertheless, the origin of the spectroscopic offset remains unclear. However, in the literature, high spectral resolution observations have indicated the presence of variations in the line profiles of CO(J = 3–2) and p-H_2O (2_{11}–2_{02}) in Mrk 232 and NGC 6240 (as depicted in fig. 2 from Liu et al. 2017), nevertheless these differences have not been explored in detail. It is worth noting that IRAS 09022-3615 has a complex morphology, as shown in Fig. C1, where the peak of MIPS 24 μm and ALMA 630 μm is not aligned with the *R*-band *HST* image.

Due to the limited spatial resolution of APEX, to fully understand the origin and powering source of the submm H_2O emission, higher angular resolution observations, such as ALMA Band-9 observations, are needed. These resolved observations need to be integrated into detailed photodissociation and radiative transfer modelling to tackle the nature of the p-H_2O (2_{11}–2_{02}) emission and provide insights on the usage of this line to describe the warm ISM in galaxies.

4 CONCLUSION

We present the first ground-based detection of the p-H_2O (2_{11}–2_{02}) emission line at 752.033 GHz in local ULIRGs using APEX SEPIA Band 9 towards IRAS 06035-7102 (z = 0.07946), IRAS 17208-0014 (z = 0.04281), and IRAS 09022-3615 (z = 0.05964). We demonstrate that despite the low transmission of the atmosphere at these high frequencies, observing this thermal water line in local galaxies can be done using ground-based facilities operating at high frequencies, reaching high signal-to-noise in a reasonable integration time (∼ 5–15 h per source) with high-spectral resolutions. For all three sources, the final APEX spectra are of high quality, improving the previous measurements done by *Herschel* SPIRE-FTS both in signal-to-noise ratios and spectral resolution, resulting in the first clear detection of this water line in IRAS 06035-7102.

We have spectrally resolved the p-H_2O (2_{11}–2_{02}) line and derived their velocity-integrated flux densities and intrinsic luminosities. We find that the H_2O emission follows the $L_{H_2O} - L_{IR}$ correlation. We compared the p-H_2O (2_{11}–2_{02}) line emission to the dust continuum at different wavelengths 100 , 630 , 850 μm and the molecular gas traced by CO(J = 3–2), CO(J = 4–3), and HCN(J = 2–1). In IRAS 06035-7102, the water emission is co-spatial with the dust emission at 850 μm and spectrally aligned with the gas traced by CO(J = 3–2). In IRAS 17208-0014, a similar behaviour is seen, where the continuum dust emission at 100 and 630 μm are spatially aligned, while in frequency space the gas traced by CO(J = 4–3) is spectrally aligned with the p-H_2O (2_{11}–2_{02}) line. In the case of IRAS 09022-3615, the p-H_2O (2_{11}–2_{02}) water emission line is redshifted by 100 $km\,s^{-1}$ as compared with the CO(J = 4–3) emission line. The origin of this offset is still inconclusive, and higher angular resolution observations are needed to understand the reasons behind this shift.

Our pilot APEX survey opens a new window for studying submm H_2O emission lines in local ULIRGs using ground-based facilities, offering better sensitivity and spectral resolution than the past space-based facilities, such as *Herschel*. Future higher spatial resolution observations, using ALMA Band-9, together with detailed radiative transfer modelling, can help us explore the distribution of the molecular gas and dust continuum in local ULIRGs to disentangle the origin of the exciting mechanism of the p-H_2O (2_{11}–2_{02}) line by reaching down to the scales of giant molecular clouds.

ACKNOWLEDGEMENTS

We are thankful to the referee, Pierre Cox, for his valuable suggestions, which have significantly enhanced the quality of this paper. DQ acknowledges support from the National Agency for Research and Development (ANID)/Scholarship Program/Doctorado Nacional/2021-21212222. CY and SA acknowledge support from the European Research Council (ERC) Advanced Grant 789410. EI acknowledges funding by ANID FONDECYT Regular 1221846. EG-A thanks the Spanish MICINN for support under projects PID2019-105552RB-C41 and PID2022-137779OB-C41. YJ acknowledges financial support from ANID BASAL project No. FB210003. This publication is based on data acquired with the Atacama Pathfinder Experiment (APEX), project ID 103.B-0471. APEX is a collaboration between the Max-Planck-Institut fur Radioastronomie, the European Southern Observatory, and the Onsala Space Observatory. This publication makes use of the following ALMA data: ADS/JAO.ALMA#2017.1.00022.S, ADS/JAO.ALMA#2018.1.00994.S ALMA is a partnership of ESO (representing its member states), NSF (USA) and NINS (Japan), together with NRC (Canada), MOST and ASIAA (Taiwan), and KASI (Republic of Korea), in cooperation with the Republic of Chile. The Joint ALMA Observatory is operated by ESO, AUI/NRAO and NAOJ. PACS has been developed by a consortium of institutes led by MPE (Germany) and including UVIE (Austria); KU Leuven, CSL, IMEC (Belgium); CEA, LAM (France); MPIA (Germany); INAF-IFSI/OAA/OAP/OAT, LENS, SISSA (Italy); IAC (Spain). This development has been supported by the funding agencies BMVIT (Austria), ESA-PRODEX (Belgium), CEA/CNES (France), DLR (Germany), ASI/INAF (Italy), and CICYT/MCYT (Spain). SPIRE has been developed by a consortium of institutes led by Cardiff University (UK) and including Univ. Lethbridge (Canada); NAOC (China); CEA, LAM (France); IFSI, Univ. Padua (Italy); IAC (Spain); Stockholm Observatory (Sweden); Imperial College London, RAL, UCL-MSSL, UKATC, Univ. Sussex (UK); and Caltech, JPL, NHSC, Univ. Colorado (USA). This development has been supported by national funding agencies: CSA (Canada); NAOC (China); CEA, CNES, CNRS (France); ASI (Italy); MCINN (Spain); SNSB (Sweden); STFC, UKSA (UK); and NASA (USA). This work is based [in part] on observations made with the *Spitzer Space Telescope*, which is operated by the Jet Propulsion Laboratory, California Institute of Technology under a contract with NASA.

DATA AVAILABILITY

The data underlying this article are available in the ESO Science Archive at https://archive.eso.org/scienceportal/home, and can be accessed with the Project ID: 103.B-0471

REFERENCES

Apostolovski Y. et al., 2019, A&A, 628, A23
Arribas S., Colina L., Monreal-Ibero A., Alfonso J., García-Marín M., Alonso-Herrero A., 2008, A&A, 479, 687
Baryshev A. M. et al., 2015, A&A, 577, A129
Belitsky V. et al., 2018, A&A, 612, A23
Berta S. et al., 2021, A&A, 646, A122
Berta S. et al., 2023, A&A, 678, A28
Bothwell M. S. et al., 2013, ApJ, 779, 67
Bradford C. M. et al., 2011, ApJ, 741, L37
CASA Team, 2022, PASP, 134, 114501
Casey C. M. et al., 2019, ApJ, 887, 55
Chu J. K. et al., 2017, ApJS, 229, 25
Clements D. L. et al., 2018, MNRAS, 475, 2097
Combes F. et al., 2012, A&A, 538, L4
Cutri R. M. et al., 2021, VizieR Online Data Catalog, p. 2328
Decarli R. et al., 2023, A&A, 673, A157
Drew P. M., Casey C. M., 2022, ApJ, 930, 142
Falstad N., González-Alfonso E., Aalto S., Fischer J., 2017, A&A, 597, A105
Farrah D. et al., 2001, MNRAS, 326, 1333
Gao Y., Solomon P. M., 2004, ApJ, 606, 271
Genzel R. et al., 1998, ApJ, 498, 579
González-Alfonso E. et al., 2010, A&A, 518, L43
González-Alfonso E., Fischer J., Aalto S., Falstad N., 2014, A&A, 567, A91
González-Alfonso E. et al., 2021, A&A, 645, A49
González-Alfonso E., Fischer J., Goicoechea J. R., Yang C., Pereira-Santaella M., Stewart K. P., 2022, A&A, 666, L3
Greve T. R. et al., 2005, MNRAS, 359, 1165
Gullberg B. et al., 2016, A&A, 591, A73
Hopwood R. et al., 2015, MNRAS, 449, 2274
Jarugula S. et al., 2019, ApJ, 880, 92
Jarugula S. et al., 2021, ApJ, 921, 97
Kim D.-C. et al., 2013, ApJ, 768, 102
Lehnert M. D., Yang C., Emonts B. H. C., Omont A., Falgarone E., Cox P., Guillard P., 2020, A&A, 641, A124
Li J. et al., 2020, ApJ, 889, 162
Lis D. C., Neufeld D. A., Phillips T. G., Gerin M., Neri R., 2011, ApJ, 738, L6
Liu L. et al., 2017, ApJ, 846, 5
Lonsdale C. J., Farrah D., Smith H. E., 2006, in Mason J. W., ed., Astrophysics Update 2. Praxis Publishing Ltd., Chichester, p. 285
Lu N. et al., 2017, ApJS, 230, 1
Mottram J. C. et al., 2014, A&A, 572, A21
Neufeld D. A., Lepp S., Melnick G. J., 1995, ApJS, 100, 132
Omont A. et al., 2011, A&A, 530, L3
Omont A. et al., 2013, A&A, 551, A115
Ott S., 2010, in Mizumoto Y., Morita K. I., Ohishi M., eds, ASP Conf. Ser. Vol. 434, Astronomical Data Analysis Software and Systems XIX. Astron. Soc. Pac., San Francisco, p. 139
Pearson C. et al., 2016, ApJS, 227, 9
Pensabene A. et al., 2021, A&A, 652, A66
Pensabene A. et al., 2022, A&A, 667, A9
Riechers D. A. et al., 2013, Nature, 496, 329
Riechers D. A. et al., 2017, ApJ, 850, 1
Sánchez-Portal M. et al., 2014, Exp. Astron., 37, 453
Sanders D. B., Mirabel I. F., 1996, ARA&A, 34, 749
Sanders D. B., Mazzarella J. M., Kim D. C., Surace J. A., Soifer B. T., 2003, AJ, 126, 1607
Solomon P. M., Vanden Bout P. A., 2005, ARA&A, 43, 677
Solomon P. M., Downes D., Radford S. J. E., Barrett J. W., 1997, ApJ, 478, 144
Stanley F., Knudsen K. K., Aalto S., Fan L., Falstad N., Humphreys E., 2021, A&A, 646, A178
van Dishoeck E. F., Herbst E., Neufeld D. A., 2013, Chem. Rev., 113, 9043
van Dishoeck E. F. et al., 2021, A&A, 648, A24
van der Werf P. P. et al., 2011, ApJ, 741, L38
Weiß A. et al., 2010, A&A, 521, L1
Yang C., Gao Y., Omont A., Liu D., Isaak K. G., Downes D., van der Werf P. P., Lu N., 2013, ApJ, 771, L24
Yang C. et al., 2016, A&A, 595, A80
Yang C. et al., 2017, A&A, 608, A144
Yang C. et al., 2019a, A&A, 624, A138
Yang J. et al., 2019b, ApJ, 880, 153
Yang C., González-Alfonso E., Omont A., Pereira-Santaella M., Fischer J., Beelen A., Gavazzi R., 2020, A&A, 634, L3

APPENDIX A: PHOTOMETRY OF THE GALAXIES

The following Table A1 presents the photometric fluxes derived from the PACS analyses at 100 and 160 μm (see Section 2.4). Data are presented together with fluxes taken from the literature.

Table A1. Multiwavelength infrared photometry for the three galaxies presented in Table 1. Flux densities are shown in Jy units.

N	*WISE* 22 μm (Jy)]	IRAS 60 μm (Jy)	PACS 70 μm (Jy)	IRAS 100 μm (Jy)	PACS 100 μm (Jy)	PACS 160 μm (Jy)	SPIRE 250 μm (Jy)	SPIRE 350 μm (Jy)	SPIRE 500 μm (Jy)
1	0.214 ± 0.001	5.13 ± 0.15	–	5.65 ± 0.28	–	–	1.23 ± 0.02	0.397 ± 0.001	0.130 ± 0.008
2	0.548 ± 0.003	31.14 ± 1.87	38.09 ± 1.74	34.90 ± 2.09	38.58 ± 0.02	23.31 ± 0.10	7.92 ± 0.04	2.95 ± 0.01	0.954 ± 0.009
3	0.430 ± 0.002	11.47 ± 0.57	12.81 ± 0.58	–	13.25 ± 0.02	8.09 ± 0.08	2.449 ± 0.007	0.823 ± 0.004	0.252 ± 0.005

Note. WISE emission at 22 μm from AllWISE Source Catalogue (Cutri et al. 2021). IRAS 60 and 100 μm measurements again retrieved from NASA/IPAC Extragalactic Database (NED). PACS emission at 70 μm from Chu et al. (2017). SPIRE emission at 250 , 350 , and 500 μm from Clements et al. (2018)

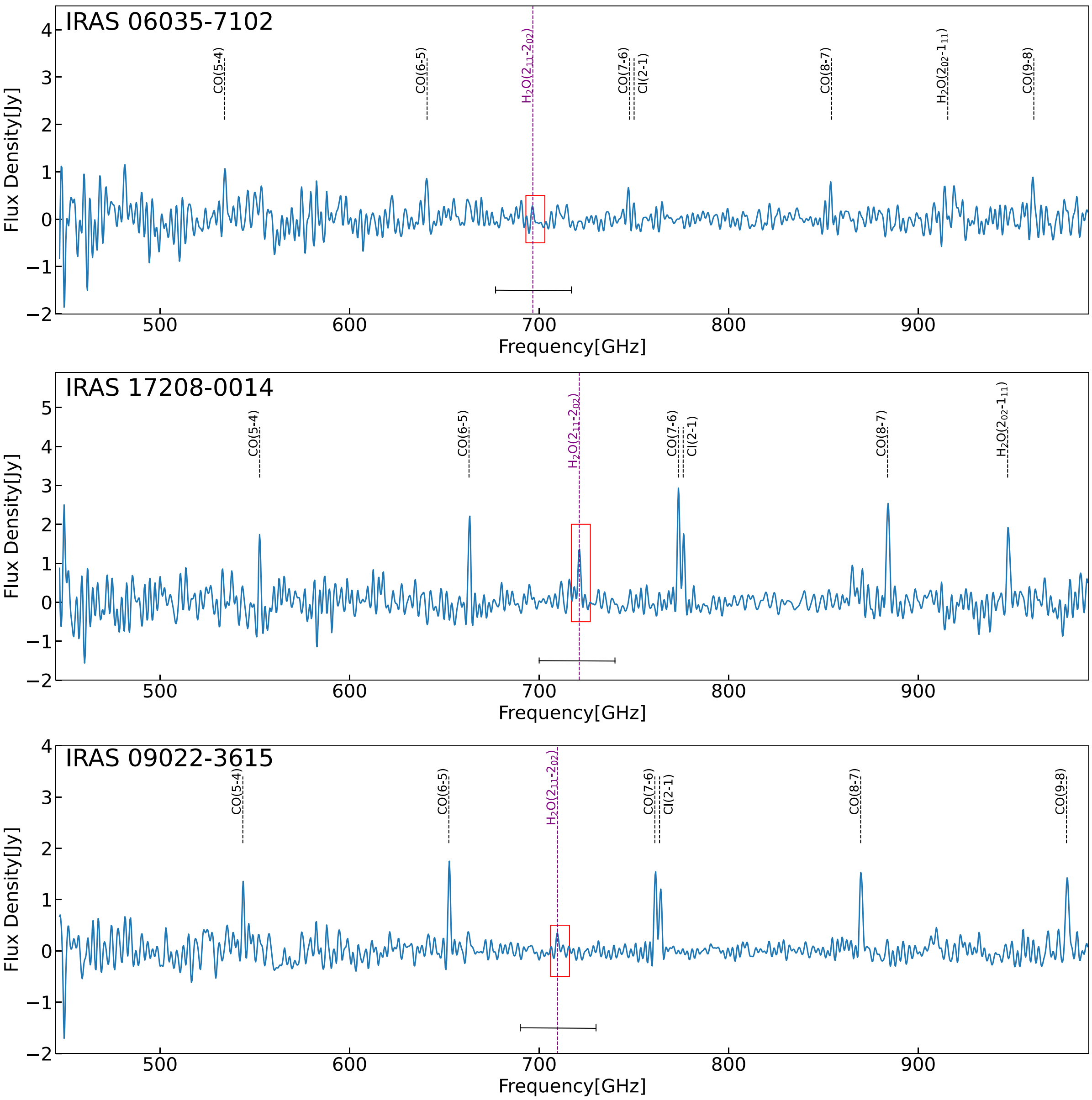

Figure B1. *Herschel* SPIRE-FTS spectra for the three sources. The segments indicate the bandwidth where we measured the RMS. The squares show the spectra taken to compare with our observations. The dashed line is p-H_2O (2_{11}–2_{02}). In IRAS 6035–7102, the water line was not detected with *Herschel* SPIRE-FTS.

APPENDIX B: *HERSCHEL* SPIRE-FTS

The following Fig. B1 presents the full spectra obtained by *Herschel* SPIRE-FTS for IRAS6035-7102, IRAS17208-0014, and IRAS09022-3615

APPENDIX C: DUST CONTINUUM

The following Fig. C1 compares different dust continuum observations towards IRAS 09022–3615. A comparison between the emission PACS 100 µm, *Spitzer*-MIPS 24 µm, and ALMA 630 µm are shown. Considering the alignment between the *Spitzer*-24 µm and ALMA-630 µm photometry, and that PACS photometry lies between these two wavelengths, the figure suggests the 2″.9 PACS offset (see Fig. 4) might be related to a calibration issue with the *Herschel* astrometry.

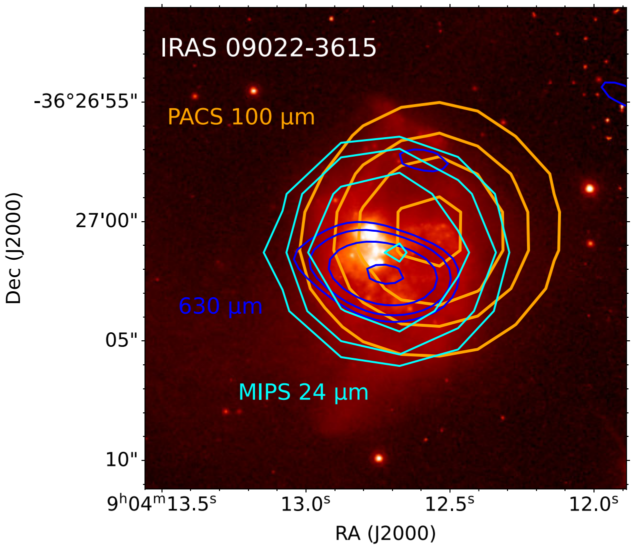

Figure C1. Different dust continuum emissions in IRAS 09022–3615 shown on top of a *Hubble Space Telescope R*-band image. The contours represent the 20 per cent, 40 per cent, 60 per cent, 90 per cent of the maximum peak intensity at 100 μm from PACS and 630 μm from ALMA and *Spitzer*-MIPS 24 μm.

This paper has been typeset from a TEX/LATEX file prepared by the author.